

High-performance p-channel transistors with transparent Zn doped-CuI

Ao Liu^{1,5}, Huihui Zhu^{1,5}, Won-Tae Park², Se-Jun Kim³, Hyungjun Kim³, Myung-Gil Kim⁴ & Yong-Young Noh¹

'Ideal' transparent *p*-type semiconductors are required for the integration of high-performance thin-film transistors (TFTs) and circuits. Although CuI has recently attracted attention owing to its excellent opto-electrical properties, solution processability, and low-temperature synthesis, the uncontrolled copper vacancy generation and subsequent excessive hole doping hinder its use as a semiconductor material in TFT devices. In this study, we propose a doping approach through soft chemical solution process and transparent *p*-type Zn-doped CuI semiconductor for high-performance TFTs and circuits. The optimised TFTs annealed at 80 °C exhibit a high hole mobility of over 5 cm² V⁻¹ s⁻¹ and high on/off current ratio of ~10⁷ with good operational stability and reproducibility. The CuI:Zn semiconductors show intrinsic advantages for next-generation TFT applications and wider applications in optoelectronics and energy conversion/storage devices. This study paves the way for the realisation of transparent, flexible, and large-area integrated circuits combined with *n*-type metal-oxide semiconductor.

¹Department of Chemical Engineering, Pohang University of Science and Technology, Pohang, Gyeongbuk 37673, Republic of Korea. ²Department of Electrical and Computer Engineering, University of Waterloo, 200 University Avenue West, Waterloo, ON N2L 3G1, Canada. ³Department of Chemistry, Korea Advanced Institute of Science and Technology, Daehak-ro 291, Yuseong-gu, Daejeon 34141, South Korea. ⁴School of Advanced Materials Science and Engineering, Sungkyunkwan University, Suwon 16419, Republic of Korea. ⁵These authors contributed equally: Ao Liu, Huihui Zhu. ✉email: myunggil@skku.edu; yynoh@postech.ac.kr

Since the commercialisation of the *n*-type metal-oxide semiconductor *a*-InGaZnO (*a*-IGZO) for thin-film transistors (TFTs) in flat panel displays in 2011, transparent *p*-type counterparts have attracted increasing interest for high-performance complementary logic circuits and next-generation ‘invisible’ active-matrix organic light-emitting diode displays^{1–4}. However, considering the industrial requirements of high mobility and optical transmittance, despite the extensive studies, the reported *p*-type metal-oxide semiconductors still exhibit insufficient performance⁵. The poor electrical properties originate from their inherent drawbacks of localised hole transport path (i.e., oxygen 2*p* orbitals) in the valence band maximum (VBM) and strong self-compensation during the doping^{6–8}. Although the concept of chemical modulation of the valence band was effective for fabricating new transparent *p*-type materials, such as CuMO₂ delafossites (M = Al, In, Ga, etc.) and LnCuOCh oxchalcogenides (Ln = lanthanide, Ch = chalcogen)^{2,9}, the low hole mobilities or high carrier concentrations and high deposition temperatures (>700 °C) make them unsuitable for transistor applications. Therefore, the search for transparent *p*-type semiconductors beyond oxides with excellent hole-transport properties and low-temperature synthesis techniques has attracted considerable interest in recent years.

To overcome the poor band dispersion of VBM with small oxide anions, alternative inorganic materials with large and easily polarisable anions have been investigated as novel *p*-type transparent semiconductors¹⁰. Among them, copper(I) iodide (CuI) is regarded the most promising candidate owing to its high intrinsic Hall mobility over 40 cm² V⁻¹ s⁻¹, high optical transparency with a wide bandgap (*E_g*) of ~3 eV, and high doping capacity with a significant *p*-type conductivity^{11,12}. CuI is consisted of abundant elements and can be synthesised at low temperatures, which enables various applications on flexible plastic substrates^{13,14}. CuI also shows diverse application potentials in thermoelectric devices, heterojunction diodes, and as a transparent conductor and hole-transport layer in photovoltaic devices^{12–19}. Initial studies on its applications as a semiconductor channel layer in TFTs have been reported recently^{20–22}. However, considering the intrinsically facile metal vacancy generation and subsequent excessive hole (*n_h* > 10¹⁹ cm⁻³), the resultant TFTs exhibited low hole mobilities and poor current modulation capabilities with low on/off current ratios (*I_{on}*/*I_{off}*) of ~10². To reduce the number of holes for the realisation of a high-performance CuI-based TFT, a feasible approach is to create donor-like iodine vacancies by thermally decomposing the lattice iodine, as demonstrated in our recent study²⁰. However, the significant iodine vacancy generation and undesired grain aggregation limited the further improvement in TFT performance and were fatal to the device operational stability.

In this study, a solution-based doping approach was proposed to screen suitable metal cations as hole suppressors for CuI with the combination of theoretical and experimental routes. Considering the ionic radius and local geometry to those of Cu⁺, Zn²⁺ was demonstrated as the champion *n*-type dopant, enabling high-performance *p*-channel TFT fabrication at 80 °C with great reproducibility over large area. The further integration of logic inverter with a *a*-IGZO TFT exhibits excellent performance with a high gain of 56.

Results

Material design of CuI with a hole-suppressor dopant. CuI has a zincblende structure below 643 K (*γ*-CuI) with intrinsic copper vacancies as hole producers at room temperature¹¹. It has a highly dispersed valence band with an effective mass of 0.3*m₀* for light holes, comparable to those of high-mobility *n*-type oxides as complementary circuit components (Supplementary Table 1).

However, the facile copper vacancy formation by the thermal stress during the fabrication or off-stoichiometry induces a significant Fermi level shift to near the VBM with a high hole concentration of 10¹⁹ cm⁻³ for the as-deposited film^{11,12,23}. To address this issue, the substitutional doping of the semiconductor with different-valence atoms can be utilised as a standard process to control the carrier concentration. The lattice structure of CuI is shown in Fig. 1a. Its VBM is characterised as a hybridisation of Cu 3*d* and I 5*p* states, while the conduction band minimum (CBM) is characterised as Cu 4*s* states (Supplementary Fig. 1a). The Cu vacancies in the CuI lattice down-shift the Fermi level, and thus create shallow defects adjacent to the VBM (upper panel of Fig. 1b). Considering the sizes and local geometries of the doped metal cations (Fig. 1c), Zn²⁺ could be an ideal dopant for CuI as a hole suppressor. Upon the Zn²⁺ doping, the defects were removed and the Fermi level was recovered to the forbidden region. Notably, this treatment produced intermediate states in the gap region as poor electron donors far from the CBM (~0.5 eV). These mid-states are characterised mostly as a hybridisation of Zn 4*s* and I 5*p* orbitals. Similar trends were observed for dopings of Pb²⁺ and Bi³⁺ at Cu⁺ sites (Supplementary Fig. 1b, c), except that the mid-states of the Bi³⁺-doped system were considerably closer to the Fermi level, far away from the CBM. This is attributed to the higher electropositivity of Bi than those of Zn and Pb, which favours the formation of the 3+ state instead of the 2+ state, and thus suppresses the creation of holes.

Consequently, our density functional theory (DFT) results suggest the control of the Fermi level location by properly choosing the dopant (among Zn²⁺, Pb²⁺, and Bi³⁺). However, the introduction of larger ions with improper coordination, such as Pb²⁺ and Bi³⁺, induces a lattice distortion near the dopant (Supplementary Fig. 2). Therefore, stable dopings of Pb²⁺ and Bi³⁺ into CuI might be challenging to achieve by typical synthesis methods.

Characterisations of doped CuI films. Various film characterisations were carried out to evaluate the doping effects of different metal cations (e.g., Zn²⁺, Ni²⁺, Pb²⁺, Bi³⁺, Ga³⁺, and Sn⁴⁺) on the film formation and properties. We focus on the Zn²⁺-doped CuI system and the results from other dopants are presented in Supplementary Information. CuI:Zn precursor solutions with different Zn²⁺ contents were prepared by mixing CuI and ZnI₂ acetonitrile solutions, followed by film coating and low-temperature annealing at 80 °C (see “Methods” section), which yielded films with negligible impurity contents (Supplementary Fig. 3). Figure 2a shows X-ray diffraction (XRD) patterns of CuI thin films doped with different cations at a concentration of 5 mol %. The preferential (111) orientation ($2\theta = 25.5^\circ$) is assigned to the *γ*-phase CuI with the zincblende structure²³. Owing to the relatively large radii of Bi³⁺ and Pb²⁺ and thus low doping efficiencies in CuI matrix, the separated BiI₃ and PbI₂ phases were detectable even with 2 mol% adding (Supplementary Fig. 4). This is consistent with the DFT calculation presented in Supplementary Fig. 2. The *p*-type conductivity of CuI mainly originates from Cu vacancies, which also affect the crystallisation²⁰. When the small amount of ZnI₂ was doped into CuI, the Zn²⁺ ions could fill or compensate Cu vacancies, which led to the improved film crystallinity (Fig. 2b). The Cu vacancy filling also slightly expanded CuI lattice, shifting the diffraction peak toward lower angle²⁴. By contrast, due to the similar ionic radii of Zn²⁺ (74 pm) and Cu⁺ (77 pm), the Zn²⁺ substitution on Cu sites kept the original lattice structure with negligible peak shift. Higher Zn²⁺ doping amounts (≥10 mol%) formed a new phase of Cu₂ZnI₄.

The X-ray photoelectron spectroscopy (XPS) results in Fig. 2c show the linearly increasing Zn 2*p* peak intensity with the Zn²⁺

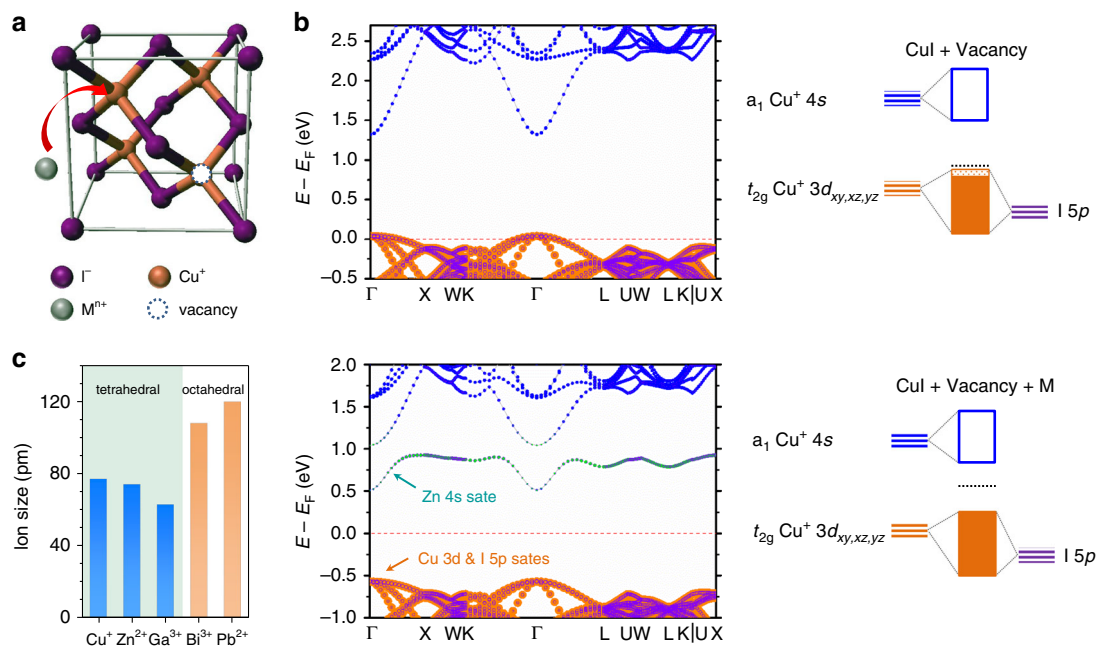


Fig. 1 DFT calculation. **a** Unit-cell of CuI and schematic of a Cu vacancy and doping at a Cu⁺ site. **b** (Upper panel) Projected band structure of CuI with a Cu vacancy content of 3%; the Cu 3d (orange), Cu 4s (blue), and I 5p (purple) states are shown. The corresponding schematic showing the orbital characteristics of the VBM and CBM is also presented. (Lower panel) Projected band structure of CuI with a Cu vacancy content of 3% and Zn²⁺ substitutional doping; the Cu 3d (orange), Cu 4s (blue), I 5p (purple), and Zn 4s (green) states are shown. The corresponding schematic showing the orbital characteristics of the VBM and CBM is also presented. **c** Radii and typical coordination of candidate dopant cations.

doping, which confirms the increased dopant concentration. The optical transmittance spectra in Supplementary Fig. 5 reveal that all CuI:Zn thin films are fully transparent in the visible region with wide bandgaps (E_g) of ~ 3 eV (Fig. 2d), which are desired for transparent electronics. The slightly increased E_g with 5-mol% Zn²⁺ doping could be attributed to the passivation of copper vacancies by Zn²⁺, which reduced the density of states in the band structure. This property is unique because the considerably declined optical transmittance was noticed after adding other dopants (Supplementary Fig. 6). The atomic force microscopy (AFM) images in Fig. 2e show the nonuniform and agglomerated surface morphology of pristine CuI with a root mean square (RMS) roughness of 1.22 nm, which could be attributed to the high volatility of acetonitrile solvent and rapid crystallisation tendency of CuI film at 80 °C. The addition of a suitable amount of Zn²⁺ effectively retarded the rapid crystallisation with a uniform grain distribution. The RMS roughness slightly increased to 1.43 and 1.60 nm for the 5- and 10-mol%-Zn-doped CuI thin films, which was mainly related to the enhanced film crystallinity. However, the further increase in Zn²⁺ doping ratio to 15 mol% led to a rough surface (RMS roughness of 5.37 nm), mainly owing to the formation of segregation phase (Supplementary Fig. 7).

The microstructures of the CuI:Zn thin films were further analysed by transmission electron microscopy (TEM), as shown in Fig. 2f and Supplementary Fig. 8. The high-resolution TEM image shows a lattice spacing of 0.348 nm for pristine CuI, which corresponds to the (111) crystalline plane of γ -phase CuI. This preferential growth orientation was verified by an in situ fast Fourier transform (FFT) pattern of the selected area. When the Zn²⁺ doping content was lower than 10 mol%, negligible variations in structure and interplanar spacing were observed and no diffraction pattern of the ZnI₂ phase could be detected. The Zn²⁺ was uniformly distributed in the composite films, according to the energy-dispersive X-ray spectroscopy (EDS) mapping and Secondary-ion mass spectrometry (SIMS) analysis (Supplementary Figs. 9 and 10). However, upon the doping of

15-mol% Zn²⁺, the continuous film changed to the combination of separated particles, which is consistent with XRD and AFM analyses.

The energy band variation of CuI thin film as a function of Zn²⁺ doping was evaluated using ultraviolet photoemission spectroscopy (UPS). As shown in Fig. 2g, the secondary electron cut-off edge shifted towards higher energies upon the Zn²⁺ addition, which indicated a Fermi energy level shift towards the conduction band edge (i.e., n -doping)²⁵. The Zn²⁺ occupation on Cu vacancies (V_{Cu} has one negative charge) and the Zn²⁺ substitution at Cu⁺ sites can generate extra electrons and thus reduce hole concentration in CuI films. The VBM calculated by using the valence region was positioned at ~ 5.25 eV, well aligned with the work function of gold electrodes ($\Phi_{Au} = 5.1$ eV) for Ohmic contact. The corresponding energy band diagrams of different Zn-doped CuI samples are presented in Fig. 2h.

Electrical characterisations of doped CuI TFTs and inverters.

To investigate the electrical properties of CuI thin films doped with different cations, a series of bottom-gate, top-contact TFTs were fabricated on SiO₂/p⁺-Si wafers with thermally evaporated Au source/drain electrodes. The optimised channel thickness is ~ 9 nm for the achievement of both high mobility and I_{on}/I_{off} (Supplementary Fig. 11). The channel layers were patterned through probe scratching to guarantee low gate leakage currents and reliable parameter extraction (Supplementary Fig. 12). The corresponding electrical characteristics are summarised in Fig. 3, Supplementary Fig. 13, and Table 2. Typical p -channel transistor behaviours were observed for all devices except for the Sn⁴⁺-doped devices (inactive). The optimal results for each dopant in Fig. 3a show that Zn²⁺ is the best dopant for CuI. The device performance as a function of Zn²⁺-doping content are summarised in Fig. 3b and Supplementary Fig. 14. A low current modulation with a high turn-on voltage (V_{on}) of ~ 40 V was observed for the 2.5-mol% Zn²⁺-doped CuI TFT, which reflected

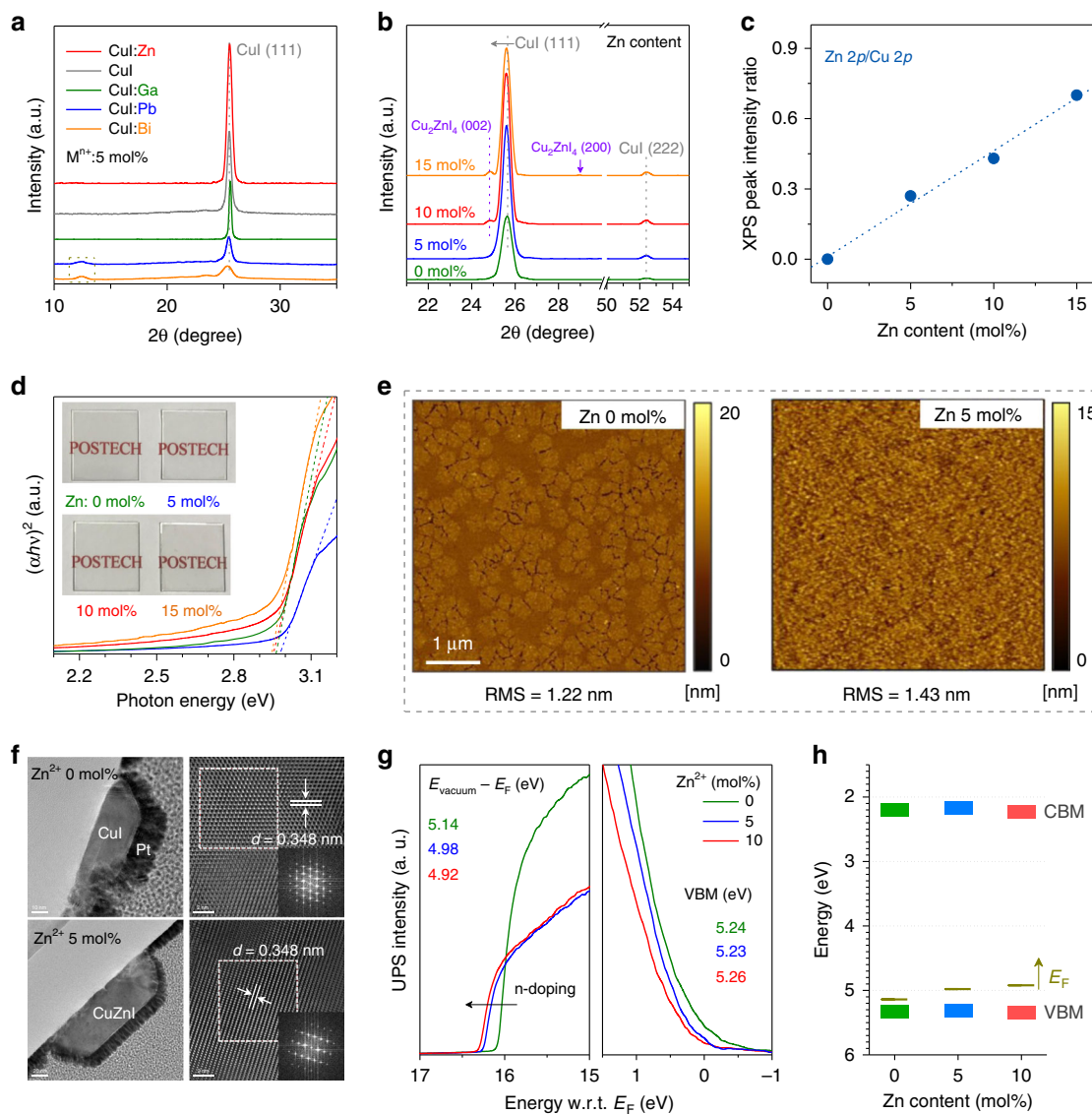


Fig. 2 Characterisations of the doped CuI thin films. **a** XRD patterns of the CuI thin films doped with different cations. **b–d** XRD patterns, XPS peak intensity ratios of Zn 2p to Cu 2p, and Tauc plots of the Zn-doped CuI films with Zn doping contents of 0–15 mol%. **e, f** AFM and TEM images (FFT pattern) of the bare and 5-mol%-Zn-doped CuI films (scale bar in HRTEM images is 2 nm). **g, h** UPS spectra of the secondary-electron onset and valence band regions and electronic energy level diagrams for the CuI:Zn thin films with different Zn²⁺ doping contents (0, 5, 10 mol%).

still high hole concentration in the channel layer. The further Zn doping reduced the current level and mobility in slope and shifted the threshold voltage (V_{TH}) in the negative direction (Fig. 3c). These trends indicate a decrease in channel conductivity with the Zn²⁺ doping, which is consistent with the UPS and DFT calculation results. The film Hall-effect measurement results also showed the declined hole concentration and mobility with Zn²⁺ doping (Supplementary Fig. 15). Overall, the TFT doped with 5-mol% Zn²⁺ (CuI:Zn_{5mol%}) exhibited well-compromised electrical performance, including a high on-state current of 1 mA, high saturation mobility (μ_{sat}) of $5.3 \pm 0.3 \text{ cm}^2 \text{ V}^{-1} \text{ s}^{-1}$, a high I_{on}/I_{off} of $\sim 10^7$, and V_{TH} of $17.5 \pm 2.0 \text{ V}$, respectively. Both mobility and I_{on}/I_{off} are record-high compared with those of previously reported solution-processed *p*-channel metal-oxide/(pseudo) halide TFTs (mobility $< 1 \text{ cm}^2 \text{ V}^{-1} \text{ s}^{-1}$ and $I_{on}/I_{off} \leq 10^4$, details in Supplementary Table 3 and Fig. 16).

Among the CuI TFTs with other dopants (Pb²⁺, Ni²⁺, Ga³⁺, Bi³⁺, Sn⁴⁺, etc.), the 5-mol% Bi³⁺ addition achieved the

optimised performances, including an effective current modulation, a μ_{sat} of $0.45 \text{ cm}^2 \text{ V}^{-1} \text{ s}^{-1}$, and an I_{on}/I_{off} of $\sim 10^4$. The inferior electrical performance compared with CuI:Zn TFTs can be attributed to the lower doping efficiency of Bi³⁺ owing to its considerably larger radius (108 pm) than that of Cu⁺ (77 pm) and improper local coordination preference (octahedral vs. tetrahedral). The scanty Bi³⁺ substitution at Cu⁺ sites could also disrupt the locally ordered CuI framework and create undesired defects, which impeded the hole transport. In addition, unusual V_{TH} 'kink' and μ_{sat} disappearance were observed for the CuI:Bi_{5mol%} TFT (Supplementary Fig. 17), which could be attributed to the voltage-induced migration of charged defects or ionic species originated from the low-crystallinity CuI and segregated BiI₃. The accumulation of dissociative ions near the electrodes could screen the applied electric field, which reduced the field-modulation capability. The ionic migration in the Bi-incorporated CuI was confirmed by scanning transfer curves at lower speeds, which led to an increased current level (Supplementary Fig. 18). Meanwhile,

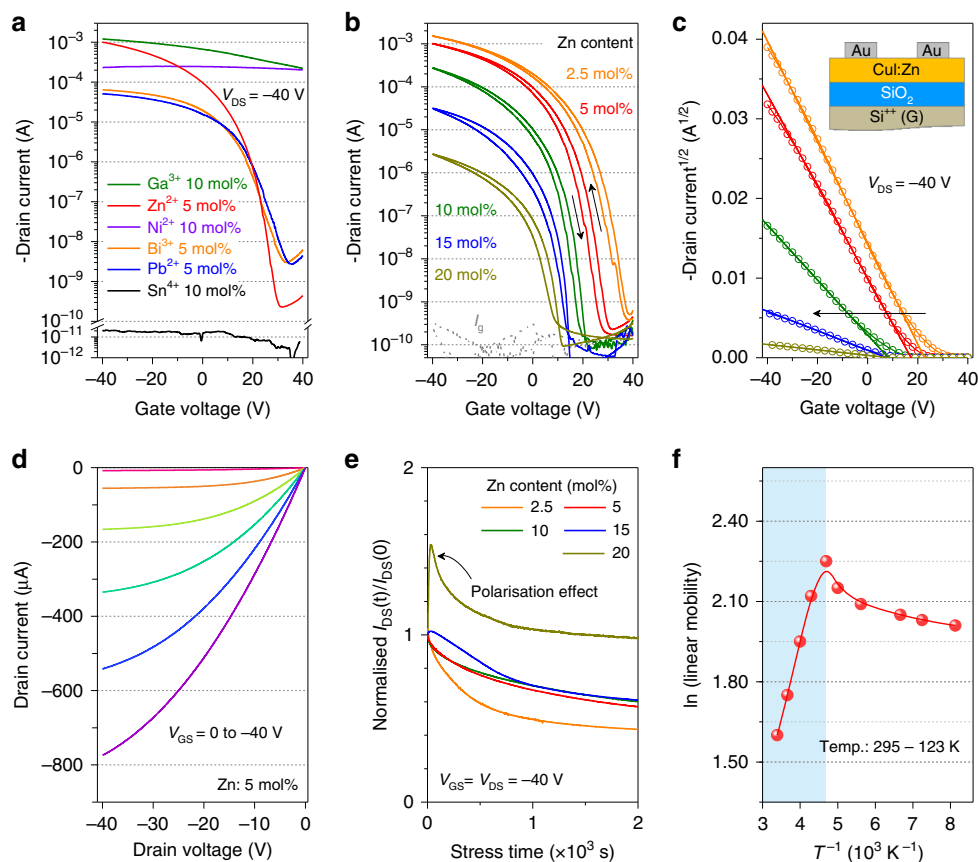


Fig. 3 Electrical performance of doped CuI TFTs. **a** Optimised transfer characteristics of the CuI TFTs doped with different cations (Ga^{3+} , Zn^{2+} , Ni^{2+} , Bi^{3+} , Pb^{2+} , and Sn^{4+}). **b, c** Transfer characteristics and $I_{\text{DS}}^{1/2}$ curves of CuI:Zn/SiO₂ TFTs with different Zn²⁺-doping contents ($V_{\text{DS}} = -40$ V). **d** Output curves of optimised CuI:Zn_{5mol%}/SiO₂ TFT. **e** Negative-bias-stress results of the CuI:Zn/SiO₂ TFTs as a function of Zn²⁺ doping content. **f** Linear mobility variation of the CuI:Zn_{5mol%}/SiO₂ TFT as a function of the temperature (295–123 K).

the μ_{sat} increased and V_{TH} shifted positively with the appearance of ‘kink’ behaviour. In contrast, the CuI:Zn TFT exhibited a stable operation with a high degree of consistency independent on the scanning speed, indicating that CuI:Zn is electrically reliable for use in transistors.

To investigate the device stabilities with Zn-doped CuI semiconductors, the operational stability under negative-bias-stress test was first carried out (Fig. 3e). The Zn²⁺ doping could effectively inhibit the drain current (I_{DS}) reduction under long-term fixed voltage application ($V_{\text{GS}} = V_{\text{DS}} = -40$ V), mainly owing to the passivation of traps, such as copper vacancies. When the Zn²⁺ doping contents were lower than 10 mol%, the I_{DS} decreased in slope under the bias stress, which was commonly observed owing to the charge trapping in the channel layer and at the channel/dielectric interface^{26–28}. The interface trap densities (D_{it} , $D_{\text{it}} = \left[\frac{SS \times \log_e}{kT/q} - 1 \right] \frac{C_{\text{it}}}{q}$), where k is the Boltzmann’s constant, T is the absolute temperature, and SS is the subthreshold swing, were calculated to be 1×10^{13} , 7.1×10^{12} , 6.7×10^{12} , 7.2×10^{12} , and $9.8 \times 10^{12} \text{ cm}^{-2}$ for 2.5-, 5-, 10-, 15-, and 20 mol% Zn²⁺-doped CuI TFTs, respectively. Notably, when the Zn²⁺ content was higher than 15 mol%, I_{DS} initially increased, and then decreased. The anomalous I_{DS} increase could be speculated by the stress-induced ionic conduction by the slow ion migration. Similar to the current variation trend, the V_{TH} shifted negatively under bias stress without obvious subthreshold swing variation (Supplementary Fig. 19). This indicated the defect state creation was negligible, and charge trapping was the dominant instability mechanism. In addition, benefiting from the large E_{g} of CuI:Zn

channel layers, the devices exhibited stable long-term operational stability under the visible light irradiation (Supplementary Fig. 20). For the CuI:Bi TFTs, owing to the low doping efficiency of Bi^{3+} in CuI matrix, the abnormal I_{DS} increase were observed in relatively long term under bias-stress tests (Supplementary Fig. 21). The air stability investigation indicated the impressionable feature of CuI:Zn semiconductor in air and the adoption of hydrophobic CYTOP passivation layer could improve the ambient durability (Supplementary Fig. 22).

The temperature-dependent measurement was then carried out to evaluate the charge transport in the CuI:Zn TFT (Fig. 3f and Supplementary Fig. 23). The mobility initially increased with the decrease in temperature from 295 to 213 K, which corresponds to the typical band-like transport behaviour^{29–31}. Such conduction was commonly observed in high-mobility semiconductors^{32–34}. The band-like transport could be attributed to the highly dispersed valence band and high degree of order in the channel layer. The subsequent mobility reduction in the lower-temperature range implies that the hole transport turned to a thermally activated transport, which could be attributed to shallow traps within grain boundaries or at the semiconductor/dielectric interface¹¹. The thermally activated hole transport was also demonstrated in other inorganic Cu-based *p*-type semiconductors (e.g., CuSCN and Cu_xO) and was the main factor for the low mobilities^{2,35,36}.

To study the scalability and uniformity of CuI:Zn TFTs, we fabricated wafer-scale TFT array (>600 TFTs) on a 4-inch Si/SiO₂ (100 nm) substrate. The photograph in Fig. 4a shows uniform film coverage over the entire substrate. 96 devices were selected

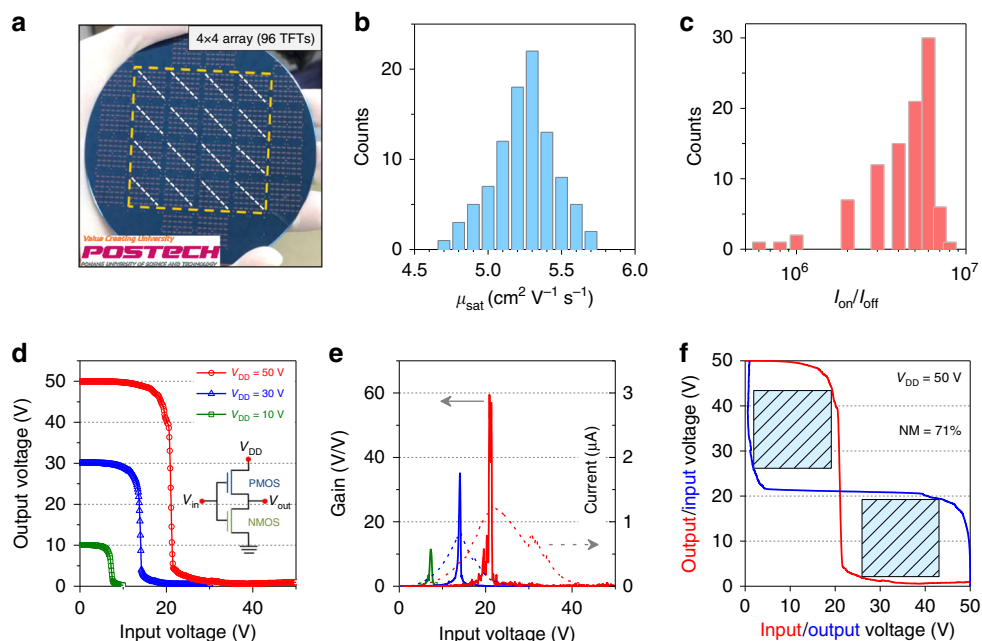


Fig. 4 Wafer-scale uniformity and the CMOS inverter integration with *n*-channel IGZO TFTs. **a** Photograph of CuI:Zn_{5mol%} TFT array on a 4-inch Si/SiO₂ (100 nm) wafer substrate (dot line means measurement area). **b, c** Statistical results of μ_{sat} and $I_{\text{on}}/I_{\text{off}}$ obtained from 96 TFTs across the array. **d–f** Voltage transfer, gain, current characteristics, and noise margin (NM) extraction of the complementary inverter based on *n*-type IGZO/SiO₂ and *p*-type CuI:Zn/SiO₂ TFTs.

and measured regularly along the dash lines and the corresponding transfer characteristics were summarized in Supplementary Fig. 24. The statistical distributions of the μ_{sat} and $I_{\text{on}}/I_{\text{off}}$ values are displayed in Fig. 4b, c. The data show high device yield with μ_{sat} of $5.3 \pm 0.5 \text{ cm}^2 \text{ V}^{-1} \text{ s}^{-1}$ and $I_{\text{on}}/I_{\text{off}}$ of 10^6 – 10^7 . The minor performance deviation is reasonable and can be related to the slight nonuniform thickness distribution in center and margin areas (<1 nm in this work) using spin-coating method. Finally, a proof-of-concept complementary inverter was assembled by cables to analyse the potentials of CuI:Zn TFTs for the realisation of high-performance logic circuits with *n*-channel *a*-IGZO devices (Supplementary Fig. 25). The voltage transfer characteristics, shown in Fig. 4d, exhibited full rail-to-rail swings and rapid voltage transitions with a high peak gain of 56 at a supply voltage (V_{DD}) of 50 V (Fig. 4e). The static currents ($V_{\text{in}} = 0 \text{ V}$ or $V_{\text{in}} = V_{\text{DD}}$) in the inverter were lower than 10 nA, which indicated that the static power consumption was smaller than 0.25 μW per logic gate (85 and 10 nW at 30 and 10 V V_{DD}). The noise margin, estimated by using the maximum equal criterion method³⁷, was higher than 70% of the ideal value ($V_{\text{DD}}/2$), which is sufficient for most static logic applications (Fig. 4f and Supplementary Fig. 26)^{38–40}. The high gain, wide logic swing window, low power consumption, and excellent noise margin show the application potentials of the CuI:Zn *p*-type semiconductor for transparent circuits. Higher CMOS inverter performance is expected by optimising the circuit geometry and CuI:Zn TFT performance.

Discussions

The above results demonstrate a new transparent inorganic *p*-type semiconductor of CuI:Zn, which enables the fabrication of high performance transistors. The thin films can be easily deposited using a one-step spin-coating process at plastic-compatible temperatures. Over the past 20 years, great efforts have been focused on *p*-type metal oxides, but we still have not realized the potential for practical applications because of too poor electrical performance, rigorous deposition process, and a lack of universality for easy repetition. Therefore, searching for

new inorganic transparent *p*-type candidates as oxide replacers should be considered. Herein, despite the initial attempt on CuI:Zn, its high transistor performance and easy processing capability exhibited great superiority when compared with previous reports. This work provides us an up-and-coming *p*-type semiconductor, which shows great compatibility with IGZO technology in the field of transparent electronics. However, the high-mobility devices were operated in depletion mode, which indicated a still high hole concentration in the channel layers. We believe that further improvements in the thin film quality (e.g., crystallinity and surface smoothness), interface modification, and device engineering will enhance the device performance and stabilities.

Conclusions

We have proposed a new transparent inorganic *p*-type semiconductor (Zn-doped CuI) by spin coating at 80 °C. The band-like charge transport and stable doping enabled the fabrication of high-performance TFTs and inverter circuits with excellent reproducibility. The results demonstrate the promising application potential of CuI:Zn as active semiconducting components via simple process for large-area, low-cost, and transparent flexible electronics. The high doping capacity enabled the adjustment of *p*-type conductivity over a wide range, which is beneficial for the applications in printable optoelectronics and energy conversion/storage.

Methods

Preparation of the precursor solution. All chemical reagents were purchased from Sigma-Aldrich and used as received without further purification. The CuI precursor solution (6 mg ml⁻¹) was prepared by dissolving a CuI powder into acetonitrile. Different doping concentrations were achieved by blending the CuI/ acetonitrile solution with a dopant (ZnI₂, GaI₃, or NiI₂)/acetonitrile solution. The volume ratio of CuI/acetonitrile to dopant/acetonitrile was 10:1. For the optimized Zn-doped component, the ZnI₂ precursor concentration is 10 mg ml⁻¹. For the dopants of BiI₃, PbI₂, and SnI₄, *N,N*-dimethylformamide was used as a solvent owing to their poor solubility in acetonitrile. The solution mixing was carried out in a glove box (N₂) under stirring for 20 min before film casting.

TFT fabrication. A bottom-gate top-contact device structure was used in the TFT fabrication. Heavily doped Si substrates with 100-nm thermally grown SiO₂ gate dielectrics were used as gate electrode and dielectric layers. Mixed precursor solutions were filtered through a 0.2- μ m syringe filter, and then spun on the plasma-treated hydrophilic SiO₂/Si substrates at 6000 rpm for 45 s. The samples were then annealed at 80 °C for 10 min with the thickness of ~9 nm. Au source and drain electrodes (40 nm) were deposited on the channel layers by thermal evaporation. The channel length and width of the shadow mask were 150 and 1000 μ m, respectively. The Cu:Zn film coating should be carried out in inert glove box or air condition with low humidity (<20%). The fabrication procedures for the solution-processed IGZO can be found in our previous report⁴¹.

Thin-film characterisations. The structures and compositions of the different Cu:Zn films were analysed by XRD (Rigaku, Ultima V) and XPS (PHI 5000 VersaProbe II). The film surface morphologies were analysed by tapping-mode AFM (Nanoscope V Multimode 8, Bruker). TEM (JEM 2100F) samples were deposited using focused ion beam (FIB). Hall measurement system (HMS-3000) was utilised to characterize the electrical property of Cu:Zn thin films. The optical transmittances of the thin films on quartz glasses were investigated by a UV-visible spectrophotometer (JASCO V-770). The optical band gap (E_g) was calculated by using the Tauc plot⁴²

$$\alpha = \frac{1}{t} \ln \left[\frac{(1-R)^2}{T} \right], \quad (1)$$

where α is the absorption coefficient

$$(ahv)^2 = A(hv - E_g), \quad (2)$$

where t is the sample thickness, T is the transmittance, and R is the reflectance, which could be neglected ($R \ll 1$).

TFT electrical measurements. Transistor measurements were performed by using a Keithley 4200 semiconductor parameter analyser in nitrogen glove box. The saturation TFT mobility was calculated as⁷

$$\mu_{\text{sat}} = \frac{2L}{WC_i} \left(\frac{\partial \sqrt{I_{\text{DS}}}}{\partial V_{\text{GS}}} \right)^2, \quad (3)$$

where L , W , and C_i are the channel length and width and dielectric areal capacitance, respectively. The activation energy (E_a) in the low-temperature analysis was computed by fitting the data by using $\mu_{\text{in}} = \mu_0 \exp(-E_a/k_B T)$, where k_B is the Boltzmann constant.

Computational methods. The first-principle DFT calculations were performed by using Vienna ab-initio simulation package (VASP)⁴³ with the Perdew–Burke–Ernzerhof exchange–correlation functional⁴⁴. The core electrons were described by using the projected-augmented-wave method⁴⁵. The plane-wave energy cut-off for the valence electrons was set to 400 eV. The d -electrons of Zn, Pb, and Bi were included as valence electrons. The reciprocal space was sampled by using a Γ -centred $2 \times 2 \times 2$ mesh. We optimised the $2 \times 2 \times 2$ supercell of γ -CuI and removed one Cu atom to create a Cu vacancy. To model the doping system, Zn, Pb, or Bi was inserted to a position far from the vacant site by replacing one Cu atom.

Data availability

All data related to this paper can be requested from the corresponding author upon reasonable request.

Received: 2 May 2020; Accepted: 20 July 2020;

Published online: 27 August 2020

References

- Nomura, K. et al. Room-temperature fabrication of transparent flexible thin-film transistors using amorphous oxide semiconductors. *Nature* **432**, 488–492 (2004).
- Kawazoe, H. et al. P-type electrical conduction in transparent thin films of CuAlO₂. *Nature* **389**, 939–942 (1997).
- Yu, X., Marks, T. J. & Facchetti, A. Metal oxides for optoelectronic applications. *Nat. Mater.* **15**, 383–396 (2016).
- Hosono, H. How we made the IGZO transistor. *Nat. Electron.* **1**, 428–428 (2018).
- Zhang, K. H., Xi, K., Blamire, M. G. & Egdell, R. G. P-type transparent conducting oxides. *J. Phys.: Condens Matter* **28**, 383002 (2016).
- Fortunato, E., Barquinha, P. & Martins, R. Oxide semiconductor thin-film transistors: a review of recent advances. *Adv. Mater.* **24**, 2945–2986 (2012).
- Wang, Z., Nayak, P. K., Caraveo-Frescas, J. A. & Alshareef, H. N. Recent developments in p-type oxide semiconductor materials and devices. *Adv. Mater.* **28**, 3831–3892 (2016).
- Liu, A. et al. Solution combustion synthesis: low-temperature processing for p-type Cu:NiO thin films for transparent electronics. *Adv. Mater.* **29**, 1701599 (2017).
- Hiramatsu, H. et al. Intrinsic excitonic photoluminescence and band-gap engineering of wide-gap p-type oxychalcogenide epitaxial films of LnCuOCh (Ln = La, Pr, and Nd; Ch = S or Se) semiconductor alloys. *J. Appl. Phys.* **94**, 5805–5808 (2003).
- Liu, A., Zhu, H. & Noh, Y.-Y. Solution-processed inorganic p-channel transistors: recent advances and perspectives. *Mater. Sci. Eng. Res.* **135**, 85–100 (2019).
- Grundmann, M. et al. Cuprous iodide—a p-type transparent semiconductor: history and novel applications. *Phys. Status Solidi A* **210**, 1671–1703 (2013).
- Yang, C., Kneiß, M., Lorenz, M. & Grundmann, M. Room-temperature synthesized copper iodide thin film as degenerate p-type transparent conductor with a boosted figure of merit. *Proc. Natl Acad. Sci. USA* **113**, 12929–12933 (2016).
- Yang, C. et al. Transparent flexible thermoelectric material based on non-toxic earth-abundant p-type copper iodide thin film. *Nat. Commun.* **8**, 16076 (2017).
- Yamada, N., Ino, R., Tomura, H., Kondo, Y. & Ninomiya, Y. High-mobility transparent p-type CuI semiconducting layers fabricated on flexible plastic sheets: toward flexible transparent electronics. *Adv. Electron. Mater.* **3**, 1700298 (2017).
- Sepalage, G. A. et al. Copper(I) iodide as hole-conductor in planar perovskite solar cells: probing the origin of J - V hysteresis. *Adv. Funct. Mater.* **25**, 5650–5661 (2015).
- Zhao, K. et al. Highly efficient organic solar cells based on a robust room-temperature solution-processed copper iodide hole transporter. *Nano Energy* **16**, 458–469 (2015).
- Schein, F.-L., von Wenckstern, H. & Grundmann, M. Transparent p-CuI/n-ZnO heterojunction diodes. *Appl. Phys. Lett.* **102**, 092109 (2013).
- Jun, T., Kim, J., Sasase, M. & Hosono, H. Material design of p-type transparent amorphous semiconductor, Cu–Sn–I. *Adv. Mater.* **30**, 1706573 (2018).
- Raj, V. et al. Introduction of TiO₂ in CuI for its improved performance as a p-type transparent conductor. *ACS Appl. Mater. Interfaces* **11**, 24254–24263 (2019).
- Liu, A. et al. Room-temperature solution-synthesized p-type copper(I) iodide semiconductors for transparent thin-film transistors and complementary electronics. *Adv. Mater.* **30**, 1802379 (2018).
- Choi, C.-H. et al. Low-temperature, inkjet printed p-type copper(i) iodide thin film transistors. *J. Mater. Chem. C* **4**, 10309–10314 (2016).
- Annadi, A., Zhang, N., Lim, D. B. K. & Gong, H. Hole transport modulations in low dimensional γ -CuI films: implication for high figure of merit and thin film transistors. *ACS Appl. Electron. Mater.* **1**, 1029–1037 (2019).
- Yamada, N., Ino, R. & Ninomiya, Y. Truly transparent p-type γ -CuI thin films with high hole mobility. *Chem. Mater.* **28**, 4971–4981 (2016).
- Xia, M. et al. Electrical and luminescence properties of Zn²⁺ doped CuI thin films. *J. Mater. Sci.: Mater. Electron.* **26**, 2629–2633 (2015).
- Paterson, A. F. et al. The impact of molecular p-doping on charge transport in high-mobility small-molecule/polymer blend organic transistors. *Adv. Electron. Mater.* **4**, 1700464 (2018).
- Liu, A., Zhu, H. & Noh, Y.-Y. Polyol reduction: a low-temperature eco-friendly solution process for p-channel copper oxide-based transistors and inverter circuits. *ACS Appl. Mater. Interfaces* **11**, 33157–33164 (2019).
- Tang, W. et al. Bias stress stability improvement in solution-processed low-voltage organic field-effect transistors using relaxor ferroelectric polymer gate dielectric. *IEEE Electron Device Lett.* **38**, 748–751 (2017).
- Park, I.-J. et al. Bias-stress-induced instabilities in p-type thin-film transistors. *IEEE Electron Device Lett.* **34**, 647–649 (2013).
- Lee, J.-S., Kovalenko, M. V., Huang, J., Chung, D. S. & Talapin, D. V. Band-like transport, high electron mobility and high photoconductivity in all-inorganic nanocrystal arrays. *Nat. Nanotechnol.* **6**, 348 (2011).
- Ji, D. et al. Band-like transport in small-molecule thin films toward high mobility and ultrahigh detectivity phototransistor arrays. *Nat. Commun.* **10**, 12 (2019).
- Kwon, S. M. et al. High-performance and scalable metal-chalcogenide semiconductors and devices via chalcogen-gel routes. *Sci. Adv.* **4**, eaap9104 (2018).
- Xu, X. et al. Electron mobility exceeding 10 cm² V⁻¹ s⁻¹ and band-like charge transport in solution-processed n-channel organic thin-film transistors. *Adv. Mater.* **28**, 5276–5283 (2016).
- Shi, Y. et al. Bottom-up growth of n-type monolayer molecular crystals on polymeric substrate for optoelectronic device applications. *Nat. Commun.* **9**, 2933 (2018).

34. Dong, R. et al. High-mobility band-like charge transport in a semiconducting two-dimensional metal-organic framework. *Nat. Mater.* **17**, 1027 (2018).
35. Jeong, C.-Y. et al. Investigation of the charge transport mechanism and subgap density of states in p-type Cu₂O thin-film transistors. *Appl. Phys. Lett.* **102**, 082103 (2013).
36. Pattanasattayavong, P., Mottram, A. D., Yan, F. & Anthopoulos, T. D. Study of the hole transport processes in solution-processed layers of the wide bandgap semiconductor copper(I) thiocyanate (CuSCN). *Adv. Funct. Mater.* **25**, 6802–6813 (2015).
37. Gelinck, G., Heremans, P., Nomoto, K. & Anthopoulos, T. D. Organic transistors in optical displays and microelectronic applications. *Adv. Mater.* **22**, 3778–3798 (2010).
38. Lin, Z. et al. Solution-processable 2D semiconductors for high-performance large-area electronics. *Nature* **562**, 254 (2018).
39. Wang, Z., Kim, H. & Alshareef, H. N. Oxide thin-film electronics using all-MXene electrical contacts. *Adv. Mater.* **30**, 1706656 (2018).
40. Wang, H. et al. Tuning the threshold voltage of carbon nanotube transistors by n-type molecular doping for robust and flexible complementary circuits. *Proc. Natl Acad. Sci. USA* **111**, 4776–4781 (2014).
41. Lee, W.-J. et al. Large-scale precise printing of ultrathin sol-gel oxide dielectrics for directly patterned solution-processed metal oxide transistor arrays. *Adv. Mater.* **27**, 5043–5048 (2015).
42. Kaushik, D. K., Selvaraj, M., Ramu, S. & Subrahmanyam, A. Thermal evaporated Copper Iodide (CuI) thin films: a note on the disorder evaluated through the temperature dependent electrical properties. *Sol. Energy Mater. Sol. C* **165**, 52–58 (2017).
43. Kresse, G. & Furthmüller, J. Efficiency of ab-initio total energy calculations for metals and semiconductors using a plane-wave basis set. *Comp. Mater. Sci.* **6**, 15–50 (1996).
44. Perdew, J. P., Burke, K. & Ernzerhof, M. Generalized gradient approximation made simple. *Phys. Rev. Lett.* **77**, 3865 (1996).
45. Blöchl, P. E. Projector augmented-wave method. *Phys. Rev. B* **50**, 17953–17979 (1994).

Acknowledgements

This study was supported by Samsung Display Corporation, the Centre for Advanced Soft-Electronics (Grant 2013M3A6A5073183), Ministry of Science and ICT through the National Research Foundation, grant-funded by the Korea government (2017R1E1A1A01075360, 2020R1A2C4001617, and 2020R1A4A1019455).

Author contributions

A.L., M.-G.K., and Y.-Y.N. designed the research and experiments. A.L. and H.H.Z. fabricated the devices. A.L., H.H.Z., and W.-T.P. performed the characterisation and analysis. S.-J.K. and H.K. performed the DFT calculation. A.L., H.H.Z., M.-G.K., and Y.-Y.N. wrote the paper. All authors contributed to the discussions. A.L. and H.H.Z. contributed equally to this study.

Competing interests

The authors declare no competing interests.

Additional information

Supplementary information is available for this paper at <https://doi.org/10.1038/s41467-020-18006-6>.

Correspondence and requests for materials should be addressed to M.-G.K. or Y.-Y.N.

Peer review information *Nature Communications* thanks the anonymous reviewers for their contribution to the peer review of this work. Peer reviewer reports are available

Reprints and permission information is available at <http://www.nature.com/reprints>

Publisher's note Springer Nature remains neutral with regard to jurisdictional claims in published maps and institutional affiliations.



Open Access This article is licensed under a Creative Commons Attribution 4.0 International License, which permits use, sharing, adaptation, distribution and reproduction in any medium or format, as long as you give appropriate credit to the original author(s) and the source, provide a link to the Creative Commons license, and indicate if changes were made. The images or other third party material in this article are included in the article's Creative Commons license, unless indicated otherwise in a credit line to the material. If material is not included in the article's Creative Commons license and your intended use is not permitted by statutory regulation or exceeds the permitted use, you will need to obtain permission directly from the copyright holder. To view a copy of this license, visit <http://creativecommons.org/licenses/by/4.0/>.

© The Author(s) 2020